

Article

Interface Synergistic Effect from Hierarchically Porous Cu(OH)₂@FCN MOF/CF Nanosheet Arrays Boosting Electrocatalytic Oxygen Evolution

Xue Li, Yinan Zheng, Hu Yao, Jiayu Bai, Siliang Yue and Xiaohui Guo *

Key Lab of Synthetic and Natural Functional Molecule Chemistry of Ministry of Education, College of Chemistry and Materials Science, Shaanxi Key Laboratory for Carbon Neutral Technology, Northwest University, Xi'an 710010, China; lxlxturbo@163.com (X.L.); zhengyinan1203@163.com (Y.Z.);

202020797@stumail.nwu.edu.cn (H.Y.); bji2418785398@stumail.nwu.edu.cn (J.B.); yuesiliang98@163.com (S.Y.)

* Correspondence: guoxh2009@nwu.edu.cn

Abstract: The electrolysis of water is an efficient and environmentally friendly technology for large-scale hydrogen production. However, the oxygen evolution reaction (OER) involves a multi-electron-proton coupling transfer step that limits the efficiency of water splitting. Therefore, there is an urgent need to develop electrocatalysts with expected activity and stability to accelerate the kinetics of the oxygen evolution reaction. In this paper, hierarchically porous Cu(OH)₂@(Fe, Co, Ni)MOF/CF nanosheet (denoted as Cu(OH)₂@FCN MOF/CF) arrays were successfully prepared by the hydrothermally induced in situ growth of FCN MOF nanosheets using modified Cu(OH)₂ nanowires as carriers; herein, the tuned active species of metal ligands in the FCN MOF composition structure are used as the main catalytic reaction site in the OER. The synergistic effect of a unique porous structure and the active metal-ligand species in the MOF render the catalyst a large electrochemically active surface area and more active species. Then, the active material is fully contacted with the electrolyte to expose more electrochemically active sites, thus greatly improving the electrocatalytic activity and durability of the OER. Specifically, the Cu(OH)₂@FCN MOF/CF delivers a minimum overpotential of 290 mV and low Tafel slope of 96.15 mV·dec⁻¹ at 10 mA·cm⁻² as well as ultra-long cycling stability. The resulted OER performance is superior to most reported MOF-based electrocatalysts. This novel structural design not only provides a new strategy for the facile preparation of low-cost and high-efficiency OER electrocatalysts but also paves an avenue for the development of other MOF-based composite electrocatalysts with excellent electrocatalytic performances.



Citation: Li, X.; Zheng, Y.; Yao, H.; Bai, J.; Yue, S.; Guo, X. Interface Synergistic Effect from Hierarchically Porous Cu(OH)₂@FCN MOF/CF Nanosheet Arrays Boosting Electrocatalytic Oxygen Evolution. *Catalysts* **2022**, *12*, 625. <https://doi.org/10.3390/catal12060625>

Academic Editors: Zhao Wang and Nicolas Alonso-Vante

Received: 7 May 2022

Accepted: 3 June 2022

Published: 7 June 2022

Publisher's Note: MDPI stays neutral with regard to jurisdictional claims in published maps and institutional affiliations.



Copyright: © 2022 by the authors. Licensee MDPI, Basel, Switzerland. This article is an open access article distributed under the terms and conditions of the Creative Commons Attribution (CC BY) license (<https://creativecommons.org/licenses/by/4.0/>).

Keywords: electrolysis; MOF; hierarchical; porous; activity; oxygen evolution reaction

1. Introduction

Increasing global energy demand and ecological issues have forced us to develop green and renewable energy conversion and storage technologies, such as water electrolysis, fuel cells and metal–air batteries. Nevertheless, owing to the sluggish electrochemical processes of oxygen evolution reaction (OER) and oxygen reduction reaction (ORR), their energy utilization and power output are terribly restricted [1–4]. To carry out these reactions efficiently, stable and highly active electrocatalysts are very essential. Hitherto, commercial ruthenium/iridium oxides for OER are still the most desirable electrocatalysts, but their practical applicability is obstructed due to their high cost, low durability and scarcity [4–10]. This is mainly attributed to the complex OER process at the anode, which is a four-electron coupled process with the presence of multiple adsorption intermediates and slow kinetics, resulting in high overpotential [9–12]. Therefore, it is very urgent to develop cost-effective, high-active and robust durability catalysts for OER in future clean-energy utilization.

In the past few decades, tremendous efforts have been devoted to the development of various nanomaterials including metal oxides, hydroxides and perovskites to replace noble

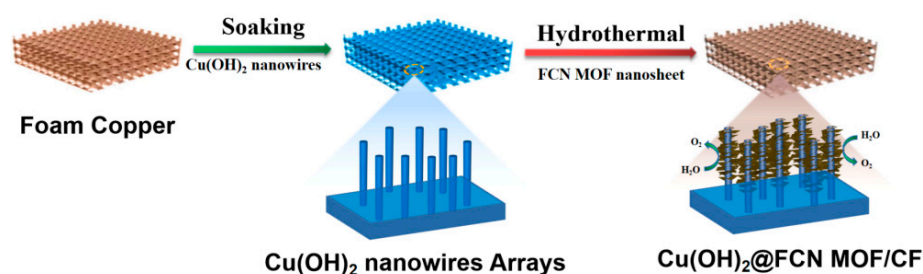
metal-based ones [11–20]. Among them, metal–organic frameworks (MOFs), can provide tunable porosity, large surface area and flexibility to be functionalized by various ligands and plentiful tailoring active sites, which can play a significant role in maximizing reaction electron transfer and facilitate reactant mass transfer, and hence, they are considered as promising electrocatalytic materials [21–26]. Although MOF and MOF-derived hybrids possess a variety of electrocatalytic properties, MOF-based electrocatalysts for direct use in OER are seldom reported, which is mainly due to their easy collapse of active nanostructure, aggregation of metal centers, and loss of active centers during high-temperature treatment processing, which leads to their reduced achievable current density and poor long-term stability [17,25–27].

Recently, some promising strategies have been employed in the design of multifunctional MOFs, including structural tuning and size/morphology control. The preparation of self-supported and efficient OER catalysts can be fabricated by in situ loading of MOFs electrocatalysts on the surface of a conductive 3D material backbone (e.g., copper foam (CF), nickel foam (NF)), which not only improves the low conductivity of the MOFs themselves but also provides a strong and tight contact between the electrocatalyst and the substrate, avoiding the use of polymer binders to ensure high exposure of the active site [4,27–29]. Ye et al. synthesized ZIF-67 loaded on nanowires $\text{Cu}(\text{OH})_2$, and the interfacial effect of $\text{Cu}(\text{OH})_2$ nanowires grown on the CF backbone expanded the surface area compared to Cu foam (CF) alone, which resulted in a more dispersed ZIF-67 favoring the contact between catalyst and electrolyte, avoiding the buildup and significantly improving the catalytic performance [30]. Xiong et al. reported an FeMOF/NiMOF/NF composite with ultrathin nanosheets that benefited from the synergistic effect of bimetallic centers, conductive substrates and unique fabrication, and hence, they exhibit impressive electrochemical properties [31]. In addition, the composite electrocatalysts based on MOF could provide more possibilities to induce synergistic effects, which also lead to the improvement of catalytic performance. The presence of synergistic effects within the structure of MOF loaded on conducting substrates was also considered as one of the main factors for developing the efficient success of MOF-based composite electrocatalysts. Therefore, the synergistic effects were explored in more depth to further improve the electrocatalytic performance of MOF materials in the OER. In addition to the MOF/substrate synergistic effects, synergistic effects acting at molecular scales in the structural composition of MOF can be further designed, such as intermolecular synergistic effects of two or more well-functioning MOF and intramolecular synergistic effects between different metal ligands of multimetal MOF structures [5]. Combining the above considerations, we aim to the in situ growth of MOF induced by conductive substrates and modulation of the species of different metal clusters within the MOFs structure by surfactant-assisted strategies in order to obtain trimetallic MOF nanosheets/ $\text{Cu}(\text{OH})_2$ nanowires heterostructure electrocatalysts with efficient electrocatalytic oxygen evolution activity.

Herein, we report a simple one-step solvothermal method for the in situ growth of $\text{Cu}(\text{OH})_2$ @FCN MOF/CF nanowire arrays for OER catalysts. The FCN MOF is in the form of nanoflakes that firmly anchored on the surface of $\text{Cu}(\text{OH})_2$ nanowires. Compared with direct growth on copper foam, the modified $\text{Cu}(\text{OH})_2$ @CF-induced in situ growth of FCN MOF nanosheets increased the active substance surface area, exposed more active sites, improved the low MOF conductivity defects and optimized the metal cluster species in the MOF nanosheets to achieve excellent electrocatalytic oxygen evolution performances. Therefore, the self-supported $\text{Cu}(\text{OH})_2$ @FCN MOF/CF nanosheets arrays demonstrate a low overpotential with of 290 mV to reach a current density of $10 \text{ mA}\cdot\text{cm}^{-2}$ in 1.0 M KOH solution, and it also exhibits remarkable long-term stability. As a result, the interesting results would highlight their potential for MOF-based electrocatalysts in future energy conversion and utilization aspects.

2. Results and Discussion

The $\text{Cu}(\text{OH})_2$ nanowires were synthesized by a room temperature immersion method. $\text{Cu}(\text{OH})_2$ nanowires were in situ grown on CF with a rapid change in substrate color from orange to blue. As shown in Scheme 1, the FCN MOF was in situ grown on the modified $\text{Cu}(\text{OH})_2$ @CF nanowire surface by a one-step solvothermal method using H_2BDC as the organic linker and $\text{FeCl}_2 \cdot 4\text{H}_2\text{O}$, $\text{CoCl}_2 \cdot 6\text{H}_2\text{O}$ and $\text{NiCl}_2 \cdot 6\text{H}_2\text{O}$ as the Fe, Co and Ni sources, respectively. In this process, Fe^{2+} is spontaneously oxidized to Fe^{3+} [32], and each BDC ligand is coordinated to six metal ions. These MO_6 ($M = \text{M1}$ or M2) octahedra are bridged by hydroxide roots along the c-axis and further coordinated by hydroxide roots and carboxyl oxygen atoms on the a and b-axes (Figure S1) [28]. The coverage of the in situ grown FCN MOF nanosheets on the backbone of the $\text{Cu}(\text{OH})_2$ @CF NWs is quite uniform as judged from the uniform color of the product (Figure 1a). For comparison, $\text{Cu}(\text{OH})_2$ @FC MOF/CF electrodes can be synthesized via simple solvothermal reaction and in the presence of two metallic (Fe and Co) precursors, and the FCN MOF/CF was also prepared without addition of the $\text{Cu}(\text{OH})_2$ @CF. The structures formed at different steps were characterized by scanning electron microscopy. In Figure S3, the $\text{Cu}(\text{OH})_2$ has a typical nanowire morphology, and the vertically grown nanowires are evenly distributed on the CF surface. In addition, the FCNMOF nanosheets were grown uniformly on the $\text{Cu}(\text{OH})_2$ @CF surface (Figure 1b), the participate in the hydrothermal reaction with CF as the substrate and FCN MOF nanosheets are stacked on the surface (Figure S3). Compared with the direct growth of CF, the unique three-dimensional structure of $\text{Cu}(\text{OH})_2$ @CF induces the FCNMOF nanosheets to grow uniformly on the surface of $\text{Cu}(\text{OH})_2$ nanowires, avoiding the accumulation and favoring the increased contact of the active material electrocatalyst with the electrolyte solution. The morphology of FCN MOF nanosheets was firstly observed by transmission electron microscopy (TEM), as shown in Figure 1c,d. In addition, EDS elemental mapping technique was utilized to further confirm the presence of Ni, Co and Fe elements on our prepared target sample, as shown in Figure 1d.



Scheme 1. Schematic illustration of the synthesis procedure of $\text{Cu}(\text{OH})_2$ @FCN MOF/CF.

To confirm the structure and surface chemical composition of the $\text{Cu}(\text{OH})_2$ @FCN MOF/CF, XRD and XPS techniques were employed to confirm this information. As shown in Figure 2a, three strong peaks at 43.4° , 50.4° and 74.2° could be indexed to the Cu substrate (JCPDS No. 04-0836), while other diffraction peaks at 16.7° , 23.8° , 34.0° , 35.8° , 38.2° , 39.8° and 53.2° correspond to the $\text{Cu}(\text{OH})_2$ (JCPDS No. 13-0420), which proved the successful formation of $\text{Cu}(\text{OH})_2$ nanowires. In addition, in the XRD pattern of $\text{Cu}(\text{OH})_2$ @FCN MOF/CF, two other characteristic diffraction peaks located at 8.9° and 17.5° can be observed that match the XRD result of FCN MOF powder, indicating that they have the same MOF structure. Upon further comparison of the XRD patterns of FCN MOF powders with the simulated powder XRD patterns of $[(\text{Co}_{1-x}\text{Fe}_x)_2(\text{OH})_2(\text{BDC})]\text{-MOF}$ [33], it was found that the FCNMOF powders display a similar crystalline feature with that of $[(\text{Co}_{1-x}\text{Fe}_x)_2(\text{OH})_2(\text{BDC})]\text{-MOF}$ (Figure S4a). As can be observed in Figure S4b, the powder X-ray diffraction patterns of all three MOFs well match each other, indicating that they have the same MOF structure. Figure S5 shows the Fourier transform infrared (FTIR) spectra of the three MOF samples. Common absorption peaks were observed at around 1585 , 1500 and 1365 cm^{-1} , which can be ascribed to the vibrations of the aromatic

carboxylate groups [34]. The peaks identified at around 1585 and 1365 cm^{-1} belong to the asymmetric and symmetric stretching vibrations of the carboxylate group, respectively. The peak located at around 3600 cm^{-1} is assigned to the O-H stretching vibrations. The two peaks at around 520 and 560 cm^{-1} are assigned to $\text{M-O}_{\text{linker}}$ vibrations [35], while the peak around 830 cm^{-1} is attributed to the $\text{M}(\mu_2\text{-OH})\text{M}$ group in all three MOFs [36].

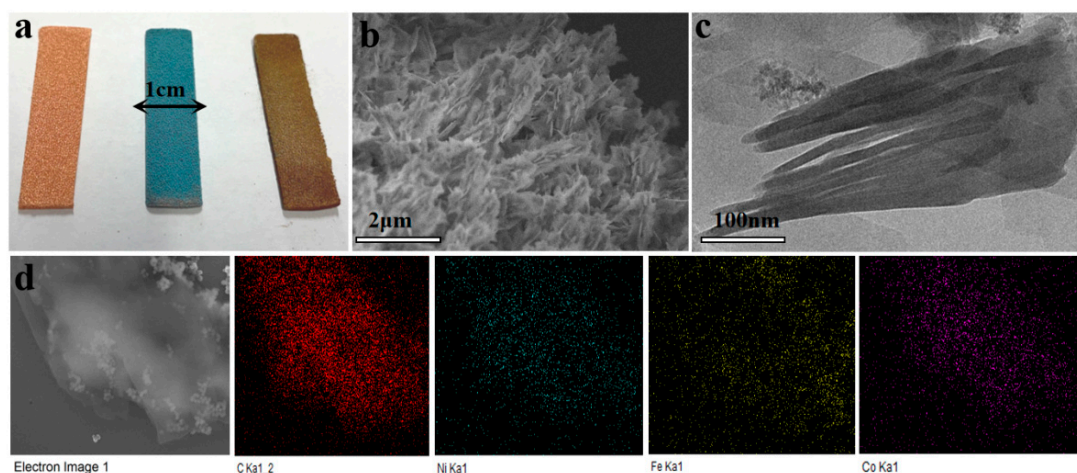


Figure 1. Morphology and composition analysis: (a) Digital photos of the stage reaction products, (b) SEM image of $\text{Cu}(\text{OH})_2@FCN\text{ MOF}/CF$, (c) TEM image of FCN MOF nanosheets with an inset of the FFT pattern of the FCN MOF nanosheets, (d) SEM image and SEM elemental mapping of FCN MOF nanosheets.

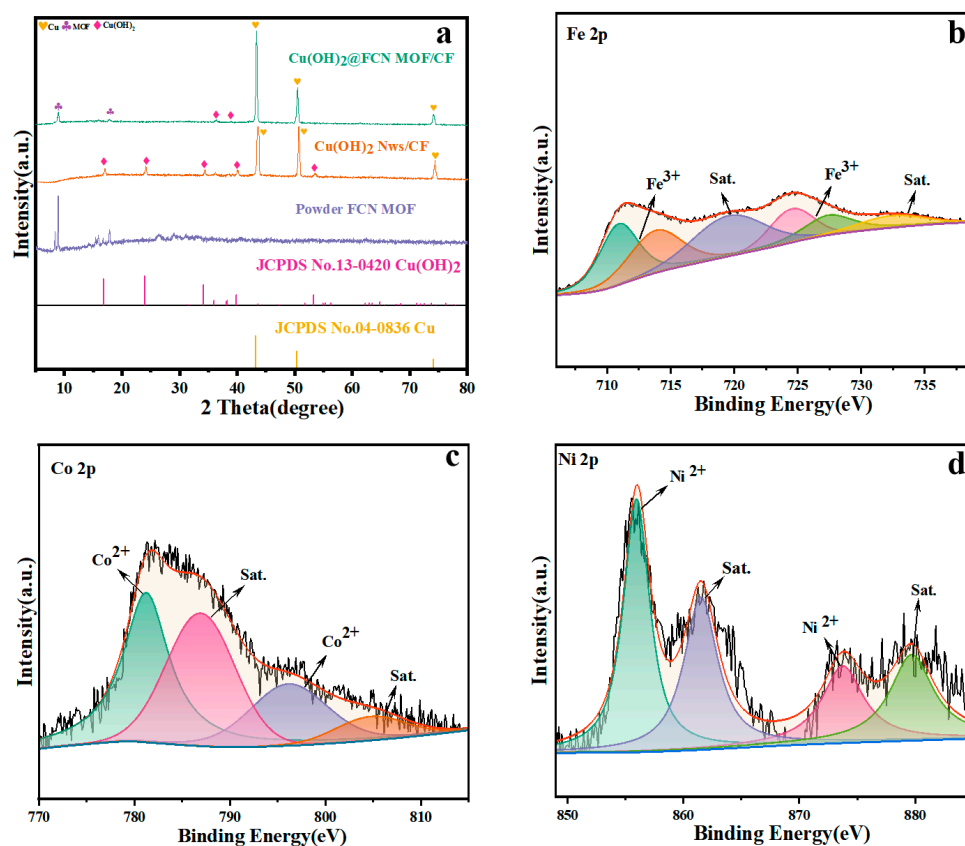


Figure 2. Structure and chemical states characterizations. (a) PXRD pattern of $\text{Cu}(\text{OH})_2@FCN\text{ MOF}/CF$, high-resolution XPS spectra of (b) Fe 2p, (c) Co 2p and (d) Ni 2p for the $\text{Cu}(\text{OH})_2@FCN\text{ MOF}/CF$ catalyst.

XPS measurements further investigate the chemical environment and surface electronic states for Cu(OH)₂@FCNMOF/CF. As presented in Figure S6, the survey XPS of Cu(OH)₂@FCNMOF/CF and Cu(OH)₂@CF NWs shows a series of signals of C 1s, O 1s, Co 2p, Fe 2p and Ni 2p. In Figure S7, the deconvolution of oxygen, the O1s spectrum was split into three peaks at 531.1 eV, which can be assigned to the C=O bond, while the other two peaks at 532.3 and 530 eV belonged to C-O and M-O [37,38]. The C 1s XPS spectrum shows that the three subpeaks at 284.3, 285.6 and 288.4 eV, which can be assigned to C-C, C-O and C=O, respectively (Figure S8) [38]. As shown in Figure S9, the Cu 2p XPS spectrum presents two main regions including Cu 2p_{1/2} and Cu 2p_{3/2}. In the Cu 2p_{1/2} region, there are two peaks located at 954.1 and 952.4 eV corresponding to the Cu²⁺ and Cu⁰ species, respectively. Similarly, the Cu 2p_{3/2} region shows the surface compositions of Cu²⁺ at 934.4 eV and Cu⁰ at 932.6 eV. However, the binding energies of Cu²⁺ and Cu⁰ were very close in the Cu 2p_{3/2} region, which could not be distinguished by XPS [39]. In addition, according to the XRD results of Cu(OH)₂@FCN MOF/CF, the existence of Cu⁰ is confirmed, which is attributed to the copper foam. The other two peaks at 962.5 and 942.3 eV can be indexed to the satellite peaks. The XPS spectra of Fe 2p signals for Cu(OH)₂@FCN MOF/CF are shown in Figure 2b. The 2p_{3/2} peaks at around 710.7 and 713.1 eV, along with the 2p_{1/2} peaks at around 724.0 and 726.0 eV, should be indexed to the Fe³⁺ species [13]. Moreover, it was found from Figure 2c that the Co 2p spectrum of the sample displayed four main peaks of Co 2p_{3/2} (781.2 eV), Co2p_{1/2} (797.2 eV) and two shake up satellite peaks (786.0 and 802.5 eV), implying the presence of Co²⁺ [40–42]. The high-resolution spectrum of Ni 2p can be reasonably deconvoluted into four peaks, as shown in Figure 2d. Two obvious peaks of Ni 2p at 856 and 873.7 eV were ascribed to Ni²⁺ 2p_{3/2} and Ni²⁺ 2p_{1/2}, respectively, and two satellite peaks were located at 861.5 and 879.7 eV [43]. The above XPS results fully evidence the formation of Cu(OH)₂@FCN MOF/CF.

The OER performance of the prepared catalysts was evaluated using a standard three-electrode configuration in a 1.0 M KOH electrolyte, in which a directly prepared sample (1 × 1 cm²), Pt electrode and Hg/HgO electrode act as the working electrode, the counter electrode and the reference electrode, respectively. It was seen from the linear sweep voltammetry (LSV) in Figure 3a that the Cu(OH)₂@FCN MOF/CF catalyst exhibits the lowest onset potential and the highest current density in comparison with CF, Cu(OH)₂@CF, RuO₂@CF, Cu(OH)₂@FCMOF/CF and Cu(OH)₂@FMOF/CF. As displayed in Figure 3c, Cu(OH)₂@FCN MOF/CF exhibits a low overpotential of 290 mV at a current density of 10 mA·cm⁻², which is optimal compared with CF (440 mV), Cu(OH)₂@CF (418 mV), Cu(OH)₂@FCMOF/CF (327 mV), Cu(OH)₂@FMOF/CF (382 mV) and RuO₂@CF (348 mV), respectively. In the LSV curve of Cu(OH)₂@FCN MOF/CF, there is a clear oxidation peak at 1.37 V vs. RHE, which should be attributed to the conversion of Ni²⁺ to Ni³⁺ during the OER process, forming Ni³⁺ as an intermediate oxidation reduction of the active substance [44]. Since the OER activity of bare Cu(OH)₂@CF is negligible, these imply that FCN MOF is the main factor that can promote the OER process. To further illustrate the interface effect of Cu(OH)₂@CF nanowire arrays with FCN MOF, in Figure S10, the Cu(OH)₂@FCN MOF/CF displays enhanced OER activity compared to FCNMOF nanosheets loaded on CF. Moreover, Cu(OH)₂@FC MOF/CF displays relative low catalytic overpotential among the six electrodes with better catalytic activity than Cu(OH)₂@F MOF/CF, which indicates that the oxygen evolution reaction is well promoted by modulating the types of metal clusters in the composition of FCN MOF nanosheets and the synergistic effect among the three metals active species.

The kinetic properties of the catalyst were further revealed by the Tafel slope, which is closely related to the rate of the electrocatalytic reaction; as shown in Figure 3b, the Tafel slope of the Cu(OH)₂@FCNMOF/CF electrode was the smallest at 96.1 mV·dec⁻¹, which was lower than that of Cu(OH)₂@FCMOF/CF (98.40 mV·dec⁻¹), Cu(OH)₂@FMOF/CF (120.77 mV·dec⁻¹), Cu(OH)₂@CF (159.79 mV·dec⁻¹), RuO₂@CF (100.71 mV·dec⁻¹) and blank CF (231.57 mV·dec⁻¹) electrodes. The improved kinetics may be attributed to the in situ growth of porous nanosheets FCN MOF on Cu(OH)₂@CF nanowire arrays, which

allows the MOF nanosheets to avoid the full exposure of stacked active sites, accelerating the mass and electron transport and thus speeding up the kinetic process.

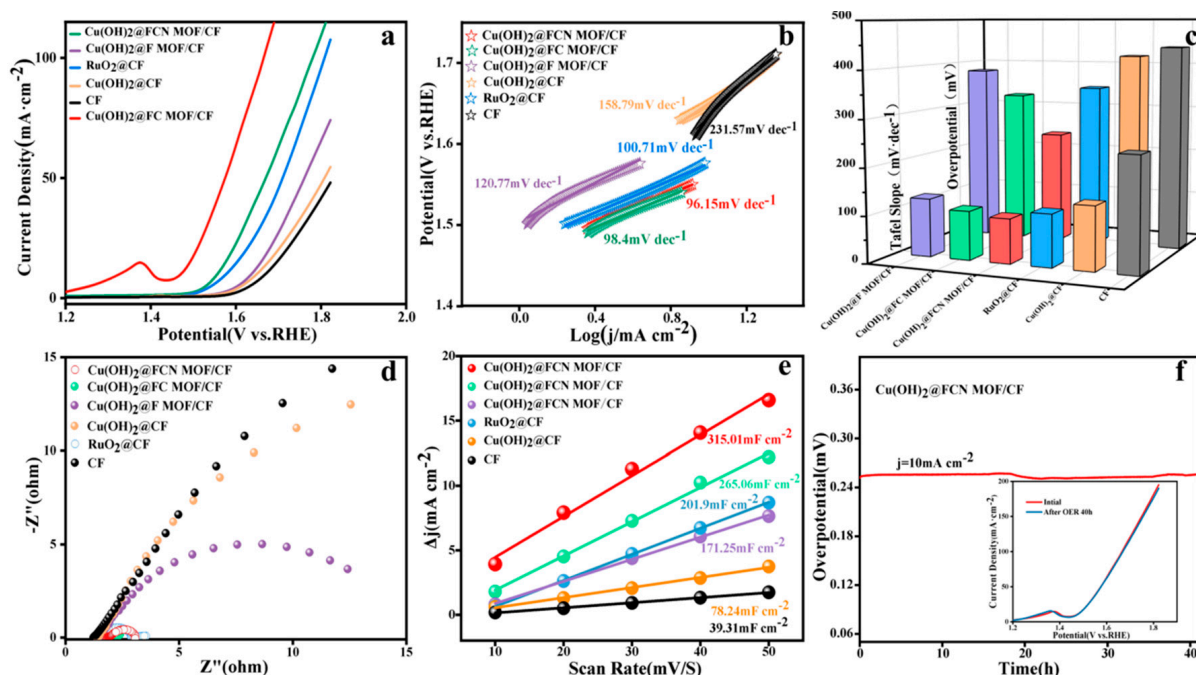


Figure 3. OER electrocatalytic performance. (a) LSV curves and (b) Corresponding Tafel plots of $\text{Cu}(\text{OH})_2@FCN\text{ MOF}/CF$, $\text{Cu}(\text{OH})_2@FC\text{ MOF}/CF$, $\text{Cu}(\text{OH})_2@F\text{ MOF}/CF$, $\text{Cu}(\text{OH})_2@CF$, CF and $\text{RuO}_2@CF$. (c) Overpotential and Tafel plots of $\text{Cu}(\text{OH})_2@FCN\text{ MOF}/CF$, $\text{Cu}(\text{OH})_2@FC\text{ MOF}/CF$, $\text{Cu}(\text{OH})_2@F\text{ MOF}/CF$, $\text{Cu}(\text{OH})_2@CF$, CF and $\text{RuO}_2@CF$. (d) Nyquist plots of $\text{Cu}(\text{OH})_2@FCN\text{ MOF}/CF$, $\text{Cu}(\text{OH})_2@FC\text{ MOF}/CF$, $\text{Cu}(\text{OH})_2@F\text{ MOF}/CF$, $\text{Cu}(\text{OH})_2@CF$, CF and $\text{RuO}_2@CF$. (e) Double-layer capacitance plots. (f) Current density curves over time at $10\text{ mA}\cdot\text{cm}^{-2}$ (inset is the polarization curves before and after 40 h OER).

To obtain a deeper insight into the partial underlying reason for the exceptional OER catalytic activity of $\text{Cu}(\text{OH})_2@FCN\text{ MOF}/CF$, electrochemical impedance spectroscopy (EIS) and the electrochemical double-layer capacitances (C_{dl}) were further studied. The charge transfer resistance (R_{ct}) is a key parameter to reveal the kinetic behavior of the catalyst and can be obtained by fitting the Nyquist plot [45]. As shown in Figure 3d, $\text{Cu}(\text{OH})_2@FCN\text{ MOF}/CF$ demonstrates the smallest semicircle diameter with an R_{ct} value of only $1.2\ \Omega$, which is much smaller than the other reference catalysts. This implies that the $\text{Cu}(\text{OH})_2@FCN\text{ MOF}/CF$ nanostructure has a quick electron transfer rate, which is consistent with the trend observed in the overpotential and Tafel slope (Figure 3c). The double layer capacitance (C_{dl}) evaluation from cyclic voltammogram (CV) curves versus different scan rates (Figure S11a) is shown in Figure 3e; the double-layer capacitance (C_{dl}) of $\text{Cu}(\text{OH})_2@FCN\text{ MOF}/CF$ is $315.01\text{ mF}\cdot\text{cm}^{-2}$, which is higher than those of $\text{Cu}(\text{OH})_2@CF$ ($78.24\text{ mF}\cdot\text{cm}^{-2}$), $\text{RuO}_2@CF$ ($209.71\text{ mF}\cdot\text{cm}^{-2}$), $\text{Cu}(\text{OH})_2@F\text{ MOF}/CF$ ($171.25\text{ mF}\cdot\text{cm}^{-2}$) and $\text{Cu}(\text{OH})_2@FC\text{ MOF}/CF$ ($265.06\text{ mF}\cdot\text{cm}^{-2}$). These results apparently show that the porous nanostructure has more active sites, the $\text{Cu}(\text{OH})_2@CF$ nanowires expand the specific surface area to avoid the direct accumulation of active material and further accelerate the transport of electrolyte ions. In addition, the trimetallic FCN MOF nanosheets array provide a large number of active centers, resulting in a much better OER performance of the $\text{Cu}(\text{OH})_2@FCN\text{ MOF}/CF$ electrode. In view of the possible errors in the experimental process, the results of this work were summarized by conducting repeatable experiments and referring to the IUPAC recommendations for valid numbers (Table S1). In addition, the turnover frequency (TOF) was determined to compare the intrinsic activity of the electrodes. The calculated TOF (Figure S12) for $\text{Cu}(\text{OH})_2@FCN\text{ MOF}/CF$,

$\text{Cu}(\text{OH})_2@FCMOF/CF$, $\text{Cu}(\text{OH})_2@FMOF/CF$ and $\text{Cu}(\text{OH})@CF$ are 0.579, 0.1897, 0.139 and 0.1 s^{-1} , respectively. These results indicate that $\text{Cu}(\text{OH})_2@FCN \text{ MOF}/CF$ exhibited higher intrinsic activity [46].

Meanwhile, the stability of the $\text{Cu}(\text{OH})_2@FCN \text{ MOF}/CF$ electrode was evaluated; the $\text{Cu}(\text{OH})_2@FCN \text{ MOF}/CF$ electrode was conducted at a current density of $10 \text{ mA}\cdot\text{cm}^{-2}$ for 40 h by the chronocurrent method. As shown in Figure 3f, $\text{Cu}(\text{OH})_2@FCN \text{ MOF}/CF$ exhibited robust durability in alkaline electrolyte with negligible performance loss after continuous 40 h operation. This indicates that the $\text{Cu}(\text{OH})_2@FCN \text{ MOF}/CF$ electrode has excellent electrochemical and mechanical stability. In addition, the structure stability of the catalyst can be further confirmed via performing the structure and morphology analysis for the cycled sample after OER, as shown in Figure S13. Herein, the excellent stability of $\text{Cu}(\text{OH})_2@FCN \text{ MOF}/CF$ is partly attributed to the in situ growth of FCN MOF on the surface of $\text{Cu}(\text{OH})_2@CF$ nanowires. The binder-free and in situ growth strategy not only improves the strong mechanical bonding and close contact between MOF and $\text{Cu}(\text{OH})_2@CF$ but also makes interaction between the uniformly dispersed and well-mixed Fe, Co and Ni ions in the FCN MOF produce a strong synergistic effect, which greatly enhances the intrinsic activity toward OER. In addition, $\text{Cu}(\text{OH})_2@FCN \text{ MOF}/CF$ has better OER catalytic performance compared with previously reported OER catalysts (Table S2) [47–55].

Based on the above analysis and discussion, the excellent OER performance of $\text{Cu}(\text{OH})_2@FCN \text{ MOF}/CF$ electrocatalysts was mainly attributed to the following factors. (i) First, there is the direct use of the trimetallic MOF as the active material; the modulation of the metal ligand species in the MOF framework leads to achieving an intramolecular synergy effect, and the preservation of the high porosity, large surface area and abundant active centers of the MOF material facilitate the improved catalytic activity. (ii) Surfactant-assisted modification of $\text{Cu}(\text{OH})_2$ nanowires anchored on the surface of FCN MOF nanosheets can effectively modulate the electronic structure of the catalyst, ensuring more exposure of active sites and significantly increasing the electrochemical active surface area, thus improving the electrochemical activity and stability. (iii) The $\text{Cu}(\text{OH})_2$ nanowires array grown on highly conductive 3D porous CF substrates ensure sufficient contact between the catalyst and electrolyte solution to promote electrolyte penetration, overcoming the drawback of the low conductivity of MOF toward electrocatalytic oxygen evolution and accelerating the mass and electron transfer.

3. Materials and Methods

3.1. Synthesis of $\text{Cu}(\text{OH})_2@CF$ NWs

The preparation of $\text{Cu}(\text{OH})_2@CF$ NWs can be realized via a facile chemical oxidation process. Namely, 2.8055 g of KOH and 0.594 g of $(\text{NH}_4)_2\text{S}_2\text{O}_8$ were mixed into a homogeneous solution, and then, a piece of CF ($1 \times 4 \text{ cm}$) was placed into the above solution for about 20 min of aging. After that, the resultant $\text{Cu}(\text{OH})_2@CF$ displays with a light blue color, after which it was washed in ethanol solution several times and dried in an oven for further use.

3.2. Surface Modification of $\text{Cu}(\text{OH})_2@CF$

The as-prepared $\text{Cu}(\text{OH})_2@CF$ NWs was modified with polyvinylpyrrolidone (PVP, $M_w \approx 24,000$) by immersing it in the DMF solution of PVP for 3 h.

3.3. Synthesis of $\text{Cu}(\text{OH})_2@FCN \text{ MOF}/CF$

Solution A: Dissolve 0.1185 g $\text{CoCl}_2\cdot 6\text{H}_2\text{O}$, 0.099 g $\text{FeCl}_2\cdot 4\text{H}_2\text{O}$, and 0.1185 g $\text{NiCl}_2\cdot 6\text{H}_2\text{O}$ in 35 mL DMF, 2.5 mL water, and 2.5 mL ethanol by ultrasound; then, add 0.249 g terephthalic acid and stir for 10 min. Solution B: Prepare 20 mL DMF, 20 mL water and 20 mL ethanol. Take 20 mL each of the above two solutions in a 100 mL Teflon-lined stainless steel autoclave and place a piece of modified ($1 \text{ cm} \times 4 \text{ cm}$) $\text{Cu}(\text{OH})_2@CF$ into the solution. After sealing, move the autoclave into an electric oven and maintain at $120 \text{ }^\circ\text{C}$ for 15 h.

Finally, rinse the resultant sample with ethanol and deionized water several times, and put it dry in an oven at 70 °C.

3.4. Synthesis of Powder FCN MOF

Solution A: Dissolve 0.1185 g $\text{CoCl}_2 \cdot 6\text{H}_2\text{O}$, 0.099 g $\text{FeCl}_2 \cdot 4\text{H}_2\text{O}$, and 0.1185 g $\text{NiCl}_2 \cdot 6\text{H}_2\text{O}$ in 35 mL DMF, 2.5 mL water, and 2.5 mL ethanol by ultrasound, add 0.249 g terephthalic acid and stir for 10 min. Solution B: Prepare 20 mL DMF, 20 mL water, and 20 mL ethanol. Take 20 mL each of the above two solutions in a 100 mL hydrothermal kettle, and heat it with water at 120 °C for 15 h. Finally, rinse it with ethanol and deionized water several times, and let it dry in an oven at 70 °C.

3.5. Characterization

The phase structure of the obtained materials was identified via X-ray powder diffractometer (XRD, Bruker D8 Advance, Bremen, Germany) equipped with Cu K α radiation. We utilize field emission scanning electron microscopy (FE-SEM, Hitachi SU8010, Japan) to observe and obtain the morphology information for our target samples. Further composition and structure information for our samples were achieved via transmission electron microscopy (TEM, FEI Talos F200X, Buxton, ME, USA) techniques. In addition, an advanced X-ray photoelectron spectroscopy (XPS, PHI5000 VersaProbe III, Tokyo, Japan) technique can further confirm the surface composition and chemical state for the prepared materials.

3.6. Electrochemical Measurements

All electrochemical measurements were connected to an electrochemical workstation (CHI660E) using a standard three-electrode system with prepared $\text{Cu}(\text{OH})_2@ \text{FCNMOF}/\text{CF}$ as the working electrode, a platinum sheet (10 mm \times 10 mm) as the counter electrode, and a commercial Hg/HgO as the reference electrode. All tests were carried out at room temperature (around 25 °C). Linear sweep voltammetry (LSV) measurements were performed in 40 mL KOH (1 M) solution with a scan rate of 1 mV/s. Cyclic voltammetry (CV) measurements were performed in 40 mL KOH solution with a scan rate of 50 $\text{mV} \cdot \text{s}^{-1}$. EIS was measured by AC impedance spectroscopy in the frequency range of 0.01–100000 Hz. The electrochemical active surface area (ECSA) was expressed by double layer capacitance (Cdl) in the potential range of 0.15–0.25 V, which was obtained from CV curves at scan rates of 10, 20, 30, 40 and 50 $\text{mV} \cdot \text{s}^{-1}$. All potentials reported in our work were calibrated relative to the reversible hydrogen electrode (RHE) using the following Nernst equation. $E(\text{RHE}) = E(\text{Hg}/\text{HgO}) + 0.059 \times \text{pH} + 0.098$. The overpotential (η) was calculated using the equation, $\eta(\text{mV}) = E(\text{RHE}) - 1.23 \text{ V}$. At a current density of 10 $\text{mA} \cdot \text{cm}^{-2}$, amperometric curve (*i*-*t*) measurements were performed to evaluate the long-term stability of the samples. All electrochemical tests were performed in the same cell configuration to ensure consistency.

4. Conclusions

In summary, $\text{Cu}(\text{OH})_2$ nanowire arrays were integrated on a conductive CF substrate by a simple room temperature immersion method. The hierarchically porous nanoarrays electrocatalysts were synthesized by the in situ growth of trimetallic MOF nanosheets via a one-pot hydrothermal method using modified $\text{Cu}(\text{OH})_2@ \text{CF}$ as a substrate. The unique hierarchical nanowires array architecture presents a larger active surface area, more active sites, adjustable electronic structure, and accelerated electron transfer rate compared with the FCN MOF that directly grows on the copper foam surface. In addition, the synergistic effect among the three metal clusters of FCN MOF and porous structure plays an important role in improving the electrocatalytic performance of the catalysts. Compared with the other synthesized comparative catalysts, $\text{Cu}(\text{OH})_2@ \text{FCNMOF}/\text{CF}$ exhibited minimum overpotential of 290 mV at a current density of 10 $\text{mA} \cdot \text{cm}^{-2}$, low Tafel slope of 96.15 $\text{mV} \cdot \text{dec}^{-1}$, and ultra-durability of 40 h. This study would facilitate

the development of efficient catalysts with fast kinetics and further promote the practical application of MOFs-based composite catalysts in energy-conversion fields.

Supplementary Materials: The following supporting information can be downloaded at: <https://www.mdpi.com/article/10.3390/catal12060625/s1>, Figure S1: The two differently coordinated metal sites (a) M1 and (b) M2 metal ions are both octahedrally coordinated to six O atoms in MOF; (a) M1 metal ion is attached to four μ -3-OH and two carboxylate oxygen atoms; (b) The M2 metal ion is linked to two μ -3-OH and four carboxylate oxygen atoms; (c) Each BDC organic ligand is coordinated to six metal ions. These MO_6 ($M = M1$ or $M2$) octahedra are bridged along the c-axis by hydrogen-oxygen and further coordinated by hydrogen-oxygen and carboxylate oxygen atoms on the a- and b-axes to form the 3D MOF. Color codes: dark blue and yellow = metal, red = oxygen, silver-white = carbon; Figure S2: SEM image of $Cu(OH)_2@CF$; Figure S3: SEM image of FCN MOF/CF; Figure S4: (a) Powder XRD patterns of $Cu(OH)_2@FCN$ MOF/CF and Powder FCNMOF; (b) Powder XRD patterns of FCN-MOF, FC-MOF, F-MOF; Figure S5: FT-IR spectra of FCN-MOF, FC-MOF, and F-MOF; Figure S6: The survey XPS spectrum of our synthesized $Cu(OH)_2@FCN$ MOF/CF and $Cu(OH)_2@CF$ samples; Figure S7: High-resolution XPS spectra of O1s of $Cu(OH)_2@FCN$ MOF/CF; Figure S8: High-resolution XPS spectra of C1s of $Cu(OH)_2@FCN$ MOF/CF; Figure S9: High-resolution XPS spectra of Cu 2p of $Cu(OH)_2@FCN$ MOF/CF; Figure S10: LSV curves of $Cu(OH)_2@FCN$ MOF/CF and Powder FCN MOF@CF; Figure S11: (a) CV curves of $Cu(OH)_2@FCN$ MOF/CF at increasing scan rates (mV/S^{-1}); (b) ECSA values of $Cu(OH)_2@MOF/CF$ catalysts with different metal species; Figure S12: (a) Reduction peak acquired for the determination of surface active MOF species; (b) Turnover frequencies (TOF) of $Cu(OH)_2@FCN$ MOF/CF, $Cu(OH)_2@FC$ MOF/CF, $Cu(OH)_2@F$ MOF/CF and $Cu(OH)_2@CF$; Figure S13: (a) Powder XRD patterns before and after OER test; (b) SEM image of $Cu(OH)_2@FCN$ MOF/CF after OER test; Table S1: Catalyst experimental error results; Table S2: Performance Comparison of $Cu(OH)_2@FCN$ MOF/CF catalysts and previously reported OER catalysts.

Author Contributions: X.L. perform the experiment and data analysis and write the manuscript draft, Y.Z. and H.Y. perform data discussion and formal analyzes, J.B. and S.Y. perform sample testing and data collection, X.G. design and supervise the project and involve results analysis, write and review the manuscript. All authors have read and agreed to the published version of the manuscript.

Funding: This work was supported by the key projects of intergovernmental international cooperation in key R & D programs of the Ministry of Science and Technology of China (No. 2021YFE0115800), the National Science Funding Committee of China (No. U20A20250), the Science and Technology Committee of Shaanxi Province (Grant No. 2020JZ-42), and China Postdoctoral Science Foundation funded project (No. 2020M673630XB).

Data Availability Statement: Data available in a publicly accessible repository that does not issue DOIs or on request from the corresponding author.

Acknowledgments: We thanks the funding support from the key projects of intergovernmental international cooperation in key R & D programs of the Ministry of Science and Technology of China, the National Science Funding Committee of China and the Science and Technology Committee of Shaanxi Province. We also specially thanks the TEM test support from the Ma Huijun.

Conflicts of Interest: The authors declare no conflict of interest.

References

1. Zhang, K.; Zou, R. Advanced Transition Metal-Based OER Electrocatalysts: Current Status, Opportunities, and Challenges. *Small* **2021**, *17*, 2100129. [[CrossRef](#)]
2. Zhang, A.; Zheng, W.; Yuan, Z.; Tian, J.; Yue, L.; Zheng, R.; Wei, D.; Liu, J. Hierarchical NiMn-layered double hydroxides@CuO core-shell heterostructure in-situ generated on $Cu(OH)_2$ nanorod arrays for high performance supercapacitors. *Chem. Eng. J.* **2020**, *380*, 122486. [[CrossRef](#)]
3. Xie, L.; Tang, C.; Wang, K.; Du, G.; Asiri, A.; Sun, X. $Cu(OH)_2@CoCO_3(OH)_2 \cdot nH_2O$ Core-Shell Heterostructure Nanowire Array: An Efficient 3D Anodic Catalyst for Oxygen Evolution and Methanol Electrooxidation. *Small* **2017**, *13*, 1602755. [[CrossRef](#)] [[PubMed](#)]
4. Chae, S.; Alagan, M.; Kim, T.; Kim, J.S.; Khil, M.S.; Lee, M.; Kim, H.; Lee, J.Y.; Kim, H.Y. Templated fabrication of perfectly aligned metal-organic framework-supported iron-doped copper-cobalt selenide nanostructure on hollow carbon nanofibers for an efficient trifunctional electrode material. *Appl. Catal. B Environ.* **2021**, *293*, 120209. [[CrossRef](#)]

5. Lin, H.; Raja, D.S.; Chuah, X.; Hsieh, C.; Chen, Y.; Lu, S. Bi-metallic MOFs possessing hierarchical synergistic effects as high performance electrocatalysts for overall water splitting at high current densities. *Appl. Catal. B Environ.* **2019**, *258*, 118023. [[CrossRef](#)]
6. Li, J.; Sun, H.; Lv, L.; Li, Z.; Ao, X.; Xu, C.; Li, Y.; Wang, C. Metal-Organic Framework-Derived Hierarchical (Co,Ni)Se₂@NiFe LDH Hollow Nanocages for Enhanced Oxygen Evolution. *ACS Appl. Mater. Interfaces* **2019**, *11*, 8106–8114. [[CrossRef](#)]
7. Ding, J.; Fan, T.; Shen, K.; Li, Y. Electrochemical synthesis of amorphous metal hydroxide microarrays with rich defects from MOFs for efficient electrocatalytic water oxidation. *Appl. Catal. B Environ.* **2021**, *292*, 120174. [[CrossRef](#)]
8. Yin, L.; Du, X.; Di, C.; Wang, M.; Su, K.; Li, Z. In-situ transformation obtained defect-rich porous hollow CuO@CoZn-LDH nanoarrays as self-supported electrode for highly efficient overall water splitting. *Chem. Eng. J.* **2021**, *414*, 128809. [[CrossRef](#)]
9. Zhou, L.; Zhang, C.; Zhang, Y.; Li, Z.; Shao, M. Host Modification of Layered Double Hydroxide Electrocatalyst to Boost the Thermodynamic and Kinetic Activity of Oxygen Evolution Reaction. *Adv. Funct. Mater.* **2021**, *31*, 2009743. [[CrossRef](#)]
10. Yang, D.; Chen, Y.; Su, Z.; Zhang, X.; Zhang, W.; Srinivas, K. Organic carboxylate-based MOFs and derivatives for electrocatalytic water oxidation. *Coord. Chem. Rev.* **2021**, *428*, 213619. [[CrossRef](#)]
11. Dai, T.; Zhang, X.; Sun, M.; Huang, B.; Zhang, N.; Da, P.; Yang, R.; He, Z.; Wang, W.; Xi, P.; et al. Uncovering the Promotion of CeO₂/CoS_{1.97} Heterostructure with Specific Spatial Architectures on Oxygen Evolution Reaction. *Adv. Mater.* **2021**, *33*, 2102593. [[CrossRef](#)]
12. Zhang, B.; Zheng, Y.; Ma, T.; Yang, C.; Peng, Y.; Zhou, Z.; Zhou, M.; Li, S.; Wang, Y.; Cheng, C. Designing MOF Nanoarchitectures for Electrochemical Water Splitting. *Adv. Mater.* **2021**, *33*, 2006042. [[CrossRef](#)]
13. Chen, C.; Tuo, Y.; Lu, Q.; Lu, H.; Zhang, S.; Zhou, Y.; Zhang, J.; Liu, Z.; Kang, Z.; Feng, X.; et al. Hierarchical trimetallic Co-Ni-Fe oxides derived from core-shell structured metal-organic frameworks for highly efficient oxygen evolution reaction. *Appl. Catal. B Environ.* **2021**, *287*, 119953. [[CrossRef](#)]
14. Liang, J.; Gao, X.; Guo, B.; Ding, Y.; Yan, J.; Guo, Z.; Tse, E.C.; Liu, J. Ferrocene-Based Metal-Organic Framework Nanosheets as a Robust Oxygen Evolution Catalyst. *Angew. Chem. Int. Ed.* **2021**, *133*, 12880–12884. [[CrossRef](#)]
15. Kang, J.; Sheng, J.; Xie, J.; Ye, H.; Chen, J.; Fu, X.; Du, G.; Sun, R.; Wong, C. Tubular Cu(OH)₂ arrays decorated with nanothorny Co-Ni bimetallic carbonate hydroxide supported on Cu foam: A 3D hierarchical core shell efficient electrocatalyst for the oxygen evolution reaction. *J. Mater. Chem. A* **2018**, *6*, 10064–10073. [[CrossRef](#)]
16. Liu, P.; Ng, V.M.H.; Yao, Z.; Zhou, J.; Lei, Y.; Yang, Z.; Kong, L.B. Facile synthesis and hierarchical assembly of flowerlike NiO structures with enhanced dielectric and microwave absorption properties. *ACS Appl. Mater. Interfaces* **2017**, *9*, 16404–16416. [[CrossRef](#)] [[PubMed](#)]
17. Liu, P.; Peng, J.; Chen, Y.; Liu, M.; Tang, W.; Guo, Z.H.; Yue, K. A general and robust strategy for in-situ templated synthesis of patterned inorganic nanoparticle assemblies. *Giant* **2021**, *8*, 100076. [[CrossRef](#)]
18. Li, H.; Liu, Y.; He, F.; Yang, H.; Li, Z.; Zhou, Q.; Tang, K. In situ grown Cu-Based metal-organic framework on copper foam as high-performance electrocatalysts for oxygen evolution reaction. *Int. J. Hydrogen Energy* **2020**, *45*, 21540–21546. [[CrossRef](#)]
19. Battiatto, S.; Urso, M.; Cosentino, S.; Pellegrino, A.L.; Mirabella, S.; Terrasi, A. Optimization of Oxygen Evolution Reaction with Electroless Deposited Ni–P Catalytic Nanocoating. *Nanomaterials* **2021**, *11*, 3010. [[CrossRef](#)] [[PubMed](#)]
20. Liu, P.; Yao, Z.; Zhou, J.; Yang, Z.; Kong, L.B. Small magnetic Co-doped NiZn ferrite/graphene nanocomposites and their dual-region microwave absorption performance. *J. Mater. Chem. C* **2016**, *4*, 9738–9749. [[CrossRef](#)]
21. Li, S.; Gao, Y.; Li, N.; Ge, L.; Bu, X.; Feng, P. Transition metal-based bimetallic MOFs and MOF-derived catalysts for electrochemical oxygen evolution reaction. *Energy Environ. Sci.* **2021**, *14*, 1897–1927. [[CrossRef](#)]
22. Wang, Y.; Liu, B.; Shen, X.; Arandiyana, H.; Zhao, T.; Li, Y.; Zhao, C. Engineering the Activity and Stability of MOF-Nanocomposites for Efficient Water Oxidation. *Adv. Energy Mater.* **2021**, *11*, 2003759. [[CrossRef](#)]
23. Qian, Q.; Li, Y.; Liu, Y.; Yu, L.; Zhang, G. Ambient Fast Synthesis and Active Sites Deciphering of Hierarchical Foam-Like Trimetal-Organic Framework Nanostructures as a Platform for Highly Efficient Oxygen Evolution Electrocatalysis. *Adv. Mater.* **2019**, *31*, 1901139. [[CrossRef](#)]
24. Ken, I.; Kenji, O.; Yasuaki, T.; Takashi, T.; Paolo, F.; Christian, J.D.; Masahide, T. MOF-on-MOF: Oriented Growth of Multiple Layered Thin Films of Metal-Organic Frameworks. *Angew. Chem. Int. Ed.* **2019**, *58*, 6960–6964.
25. Zhou, J.; Dou, Y.; Zhou, A.; Shu, L.; Chen, Y.; Li, J.R. Layered Metal–Organic Framework-Derived Metal Oxide/Carbon Nanosheet Arrays for Catalyzing the Oxygen Evolution Reaction. *ACS Energy Lett.* **2018**, *3*, 1655–1661. [[CrossRef](#)]
26. Qin, Y.; Han, X.; Li, Y.; Han, A.; Liu, W.; Xu, H.; Liu, J. Hollow Mesoporous Metal–Organic Frameworks with Enhanced Diffusion for Highly Efficient Catalysis. *ACS Catal.* **2020**, *10*, 5973–5978. [[CrossRef](#)]
27. Li, D.J.; Li, Q.H.; Gu, Z.G.; Zhang, J. A surface-mounted MOF thin film with oriented nanosheet arrays for enhancing the oxygen evolution reaction. *J. Mater. Chem. A* **2019**, *7*, 18519–18528. [[CrossRef](#)]
28. Raja, D.S.; Huang, C.L.; Chen, Y.A.; Choi, Y.M.; Lu, S.Y. Composition-balanced trimetallic MOFs as ultra-efficient electrocatalysts for oxygen evolution reaction at high current densities. *Appl. Catal. B Environ.* **2020**, *279*, 127111.
29. Raja, D.S.; Chuah, X.F.; Lu, S.Y. In Situ Grown Bimetallic MOF-Based Composite as Highly Efficient Bifunctional Electrocatalyst for Overall Water Splitting with Ultrastability at High Current Densities. *Adv. Energy Mater.* **2018**, *8*, 1801065. [[CrossRef](#)]
30. Ye, L.; Zhang, Y.; Wang, L.; Zhao, L.; Gong, Y. Assembly of ZIF-67 nanoparticles and in situ grown Cu(OH)₂ nanowires serves as an effective electrocatalyst for oxygen evolution. *Dalton Trans.* **2021**, *50*, 7256–7264. [[CrossRef](#)] [[PubMed](#)]

31. Xiong, D.; Gu, M.; Chen, C.; Lu, C.; Yi, F.; Ma, X. Rational design of bimetallic metal–organic framework composites and their derived sulfides with superior electrochemical performance to remarkably boost oxygen evolution and supercapacitors. *Chem. Eng. J.* **2021**, *404*, 127111. [[CrossRef](#)]
32. Li, F.L.; Wang, P.; Huang, X.; Young, D.J.; Wang, H.F.; Braunstein, P.; Lang, J.P. Large-Scale, Bottom-Up Synthesis of Binary Metal–Organic Framework Nanosheets for Efficient Water Oxidation. *Angew. Chem. Int. Ed.* **2019**, *58*, 7051–7056. [[CrossRef](#)] [[PubMed](#)]
33. Adel, M.; Bernard, M.; Thomas, M.; Romain, S.; Michel, F. Location of metallic elements in $(\text{Co}_{1-x}\text{Fe}_x)_2(\text{OH})_2(\text{C}_8\text{H}_4\text{O}_4)$: Use of MAD, neutron diffraction and ^{57}Fe Mössbauer spectroscopy. *CrystEngComm* **2010**, *12*, 3126–3131.
34. Huang, Z.L.; Drillon, M.; Masciocchi, N.; Sironi, A.; Zhao, J.T.; Rabu, P.; Panissod, P. Ab-initio XRPD crystal structure and giant hysteretic effect ($H_c = 5.9$ t) of a new hybrid terephthalate-based cobalt(II) magnet. *Chem. Mater.* **2000**, *12*, 2805–2812. [[CrossRef](#)]
35. Sun, Q.; Liu, M.; Li, K.; Han, Y.; Zuo, Y.; Chai, F.; Song, C.; Zhang, G.; Guo, X. Synthesis of Fe/M (M = Mn, Co, Ni) bimetallic metal organic frameworks and their catalytic activity for phenol degradation under mild conditions. *Inorg. Chem. Front.* **2017**, *4*, 144–153. [[CrossRef](#)]
36. Nouar, F.; Devic, T.; Chevreau, H.; Guillou, N.; Gibson, E.; Clet, G.; Daturi, M.; Vimont, A.; Grenèche, J.M.; Breeze, M.I.; et al. Tuning the breathing behaviour of MIL-53 by cation mixing. *Chem. Commun.* **2012**, *48*, 10237–10239. [[CrossRef](#)]
37. Yaqoob, L.; Noor, T.; Iqbal, N.; Nasir, H.; Zaman, N.; Talha, K. Electrochemical synergies of Fe–Ni bimetallic MOF CNTs catalyst for OER in water splitting. *J. Alloys Compd.* **2021**, *850*, 156583. [[CrossRef](#)]
38. McIntyre, N.S.; Zetaruk, D.G. X-ray photoelectron spectroscopic studies of iron oxides. *Anal. Chem.* **2002**, *49*, 1521–1529. [[CrossRef](#)]
39. Tang, Y.J.; Wang, Y.; Zhu, H.J.; Zhou, K.; Lan, Y.Q. In situ growth of a POMOF-derived nitride based composite on Cu foam to produce hydrogen with enhanced water dissociation kinetics. *J. Mater. Chem. A* **2019**, *7*, 13559–13566. [[CrossRef](#)]
40. Tan, B.J.; Klabunde, K.J.; Sherwood, P.M. XPS studies of solvated metal atom dispersed (SMAD) catalysts. Evidence for layered cobalt-manganese particles on alumina and silica. *J. Am. Chem. Soc.* **1991**, *3*, 855–861. [[CrossRef](#)]
41. Bonnelle, J.P.; Grimblot, J.; D’huysser, A. Influence de la polarisation des liaisons sur les spectres esca des oxydes de cobalt. *J. Electron. Spectrosc. Relat. Phenom.* **1975**, *7*, 151–162. [[CrossRef](#)]
42. Strydom, C.A.; Strydom, H.J. X-ray photoelectron spectroscopy studies of some cobalt (II) nitrate complexes. *Inorg. Chim. Acta.* **1989**, *159*, 191–195. [[CrossRef](#)]
43. Yuan, C.Z.; Sun, Z.T.; Jiang, Y.F.; Yang, Z.K.; Jiang, N.; Zhao, Z.W.; Qazi, U.Y.; Zhang, W.H.; Xu, A.W. One-Step In Situ Growth of Iron-Nickel Sulfide Nanosheets on FeNi Alloy Foils: High-Performance and Self-Supported Electrodes for Water Oxidation. *Small* **2017**, *13*, 1604161. [[CrossRef](#)] [[PubMed](#)]
44. Thenuwara, A.C.; Cerkez, E.B.; Shumlas, S.L.; Attanayake, N.H.; McKendry, I.G.; Frazer, L.; Strongin, D.R. Nickel confined in the interlayer region of birnessite: An active electrocatalyst for water oxidation. *Angew. Chem. Int. Ed.* **2016**, *128*, 10537–10541. [[CrossRef](#)]
45. Jadhav, H.S.; Bandal, H.A.; Ramakrishna, S.; Kim, H. Critical Review, Recent Updates on Zeolitic Imidazolate Framework-67 (ZIF-67) and Its Derivatives for Electrochemical Water Splitting. *Adv. Mater.* **2022**, *34*, 2107072. [[CrossRef](#)]
46. Anantharaj, S.; Ede, S.R.; Karthick, K.; Sankar, S.S.; Sangeetha, K.; Karthik, P.E.; Kundu, S. Precision and correctness in the evaluation of electrocatalytic water splitting: Revisiting activity parameters with a critical assessment. *Energy Environ. Sci.* **2018**, *11*, 744–771. [[CrossRef](#)]
47. Chang, Y.; Zhai, P.; Hou, J.; Zhao, J.; Gao, J. Excellent HER and OER Catalyzing Performance of Se-Vacancies in Defects-Engineered PtSe₂: From Simulation to Experiment. *Adv. Energy Mater.* **2022**, *12*, 2102359. [[CrossRef](#)]
48. Gong, W.; Zhang, H.; Yang, L.; Yang, Y.; Wang, J.; Liang, H. Core@shell MOFs derived Co₂P/CoP@NPGC as a highly-active bifunctional electrocatalyst for ORR/OER. *J. Ind. Eng. Chem.* **2022**, *106*, 492–502. [[CrossRef](#)]
49. Liu, Z.; Wan, J.; Li, M.; Shi, Z.; Liu, J.; Tang, Y. Synthesis of Co/CeO₂ hetero-particles with abundant oxygen-vacancies supported by carbon aerogels for ORR and OER. *Nanoscale* **2022**, *14*, 1997–2003. [[CrossRef](#)]
50. Silva, V.D.; Ferreira, L.S.; Simões, T.A.; Medeiros, E.S.; Macedo, D.A. 1D hollow MFe₂O₄ (M = Cu, Co, Ni) fibers by Solution Blow Spinning for oxygen evolution reaction. *J. Colloid Interface Sci.* **2019**, *540*, 59–65. [[CrossRef](#)] [[PubMed](#)]
51. Swathi, S.; Yuvakkumar, R.; Ravi, G.; Al-Sehemibc, A.G.; Velauthapillai, D. Rare earth metal (Sm)-doped NiMnO₃ nanostructures for highly competent alkaline oxygen evolution reaction. *Nanoscale Adv.* **2022**, *4*, 2235–2358. [[CrossRef](#)]
52. Yang, B.; Chang, X.; Ding, X.; Ma, X.; Zhang, M. One-dimensional Ni₂P/Mn₂O₃ nanostructures with enhanced oxygen evolution reaction activity. *J. Colloid Interface Sci.* **2022**, *625*, 196–204. [[CrossRef](#)]
53. Jiang, H.; He, Q.; Li, X.; Su, X.; Zhang, Y.; Chen, S.; Zhang, S.M.; Zhang, G.; Jiang, J.; Luo, Y.; et al. Tracking Structural Self-Reconstruction and Identifying True Active Sites toward Cobalt Oxochloride Precatalyst of Oxygen Evolution Reaction. *Adv. Mater.* **2019**, *31*, 1805127. [[CrossRef](#)]
54. Guo, Y.; Sun, Q.; Huang, Q.; Hu, Y.; Su, K.; Li, T.T.; Qian, J. Variable HOF-derived carbon-coated cobalt phosphide for electrocatalytic oxygen evolution. *Carbon* **2022**, *196*, 457–465. [[CrossRef](#)]
55. Huang, Q.Q.; Zhang, L.L.; Wu, P.; Zhang, M.C.; Liu, J.L.; Wu, J.S.; Ren, X.M. The morphology, crystal structure and oxygen evolution reaction electrocatalysis performance of scandium-doped MIL-101 (Fe). *J. Solid State Chem.* **2022**, *312*, 123202. [[CrossRef](#)]